Chemical Science

Accepted Manuscript

This article can be cited before page numbers have been issued, to do this please use: A. Paikar, P. Thai, M. T. Figgins, B. Mandal, M. Lekas, J. Reibenspies, G. V. Trieste and D. C. Powers, *Chem. Sci.*, 2026, DOI: 10.1039/D6SC02258H.

ROYAL SOCIETY OF CHEMISTRY

rsc.li/chemical-science

View Article Online
DOI: 10.1039/D6SC02258H

ARTICLE

Synthesis, Characterization, and Imidogen Photochemistry of a Hydrazoic Acid Adduct of Rh_2

Received 00th January 20xx,
Accepted 00th January 20xx

DOI: 10.1039/x0xx00000x

Arpan Paikar, Phong Thai, Matthew T. Figgins, Bodhisattwa Mandal, Matthew J. Lekas, Joseph H. Reibenspies, Gerard P. Van Trieste, and David C. Powers*

Metal–imidogen (*i.e.*, M–NH) intermediates are proposed in metal-catalyzed NH-transfer reactions. Transition metal complexes of hydrazoic acid (HN_3) could serve as precursors to these transient intermediates; however, the coordination chemistry of HN_3 is essentially unknown. Here, we report the synthesis and characterization of $Rh_2(esp)_2(HN_3)_2$, the first crystalline transition metal complex of HN_3 (esp = α,α,α′,α′-tetramethyl-1,3-benzenedipropionate). Temperature-dependent multi-nuclear NMR, UV-vis, and IR spectroscopies demonstrate that HN_3 is a weakly coordinating ligand ($K_{eq} = 1100 \pm 100$ M^{-2} at 243 K). Cryogenic photolysis (77 K) enabled observation of a non-steady state intermediate, which we assign to be a triplet Rh_2–NH complex, that engages in olefin aziridination chemistry. The nitrene photochemistry of $Rh_2(esp)_2(HN_3)_2$ was corroborated by *in crystallo* synthesis and cryogenic spectroscopic characterization of a family of *N*-aryl nitrene complexes. Together, these results establish the coordination chemistry of HN_3, confirm the triplet ground state of the Rh_2–NH intermediate responsible for catalytic NH transfer, and demonstrate a photochemical platform to observe intermediates in NH-transfer catalysis.

Introduction

Imidogen (*i.e.*, NH) is the simplest nitrene and cryogenic matrix isolation has established its triplet ground state (*i.e.*, ^{3}[NH]).[1-4] Conceptually, imidogen transfer to C–H bonds and olefins would streamline access to primary amines and N–H aziridines, respectively.[5-9] In the absence of a catalyst, NH transfer is rarely observed: Even at low temperature (~20 K), imidogen dimerizes to generate N_2H_2[10,11] and reacts unselectively with olefinic substrates to yield mixtures of HCN, N_2, and alkyl nitriles (Figure 1a).[12,13] Significant progress has been made towards the development of Rh_2-,[14, 15] Co-,[16] and Fe-catalyzed[5, 17, 18] NH-transfer reactions, although at present, optimization of these reactions is empirically guided because the putative M–NH intermediates have eluded experimental observation.

Hydrazoic acid (HN_3) — the simplest molecular azide — is an explosive, toxic, and volatile liquid (b.p. = 310 K (37 °C)).[19] HN_3 is monomeric in the gas phase[10, 20-23] and displays a tetrameric structure in the solid state that persists up to its melting point (190(5) K).[24, 25] HN_3 can serve as a precursor to imidogen via photochemical N_2 extrusion.[22, 26-28] Application of HN_3 photochemistry to the preparation of reactive M–NH complexes is currently stymied by the lack of HN_3 coordination chemistry. In 1970, Schmidt suggested that reaction of HN_3 with $SbCl_5$ — which ultimately affords NH_4SbCl_6, $[SbCl_4(N_3)]_2$, and N_2 — proceeds through an unobserved $HN_3{\cdot}SbCl_5$ adduct.[29] Oxidative addition of HN_3 with vanadium, chromium, and digermanium complexes have been observed and suggested to proceed via unobserved HN_3 adducts.[30-32] In 2019, Schulz reported the first — and thus far only — example of a crystalline HN_3 coordination compound, $HN_3{\cdot}B(C_6F_5)_3$ (Figure 2a).[33] Above 253 K (−20 °C), N_2 loss is facile and results in aminoborane formation. The complete lack of transition metal complexes of HN_3 prevents experimental evaluation of potential imidogen transfer chemistry from these platforms.

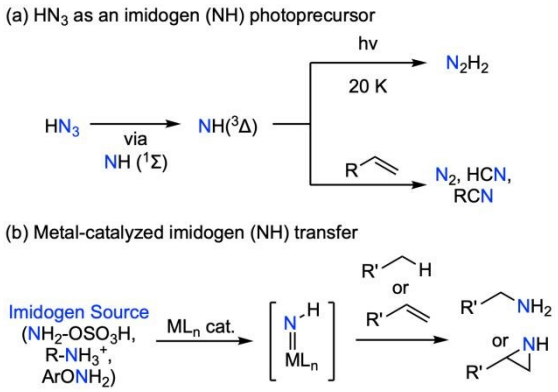

Figure 1. (a) Photochemical synthesis of ^{3}[NH] from HN_3. ^{3}[NH] dimerizes to generate N_2H_2 and reacts with olefins to afford mixtures of nitrogen-containing products. (b) Metal-catalyzed imidogen-transfer reactions have been developed for both C–H amination and olefin aziridination.

$Rh_2(esp)_2$ (**1**) catalyzes NH-transfer from hydroxylamine derivatives to olefinic substrates and Rh_2(II,II)–NH intermediates have been proposed intermediates.[14, 15] Computational studies have suggested the proposed Rh_2(II,II)–NH adopts a triplet ground state.[34, 35] Rh_2(II,III) intermediates have been suggested as alternative intermediates,[36-38] in part based on the facility of one-electron

Department of Chemistry, Texas A&M University, College Station, Texas 77843, United States: E-mail: powers@chem.tamu.edu

Electronic Supplementary Information (ESI) available: Experimental procedures, spectral data, Cartesian coordinates for the calculated structures, and X-ray diffraction details. See DOI: 10.1039/x0xx00000x

hydroxylamine redox chemistry.[39] To investigate the putative Rh_2-imidogen intermediates and establish photochemical access to M–NH species, here, we report the synthesis and characterization of the first crystalline transition metal complex of hydrazoic acid, $Rh_2(esp)_2(HN_3)_2$ (**2**) (Figure 2b). Complex **2** is prepared by treatment of **1** with HN_3 and is characterized by single-crystal X-ray diffraction (SCXRD), ^{1}H, ^{13}C, and ^{15}N NMR, IR, and UV-vis spectroscopies. Photolysis of **2** in the presence of olefinic substrates promotes stereospecific NH transfer and cryogenic photolysis suggests the intermediacy of a transient triplet Rh_2 imidogen adduct (*i.e.*, ^{3}[Rh_2–NH]). The obtained spectroscopic data were further corroborated by *in crystallo* synthesis and spectroscopic characterization of a family of Rh_2 *N*-aryl nitrene complexes. These findings indicate the chemical and kinetic competence of ^{3}[Rh_2–NH] intermediates in NH-transfer catalysis, detail the first spectroscopic characterization of Rh_2 nitrenes, and introduce new opportunities in the synthesis of reactive M–NH intermediates.

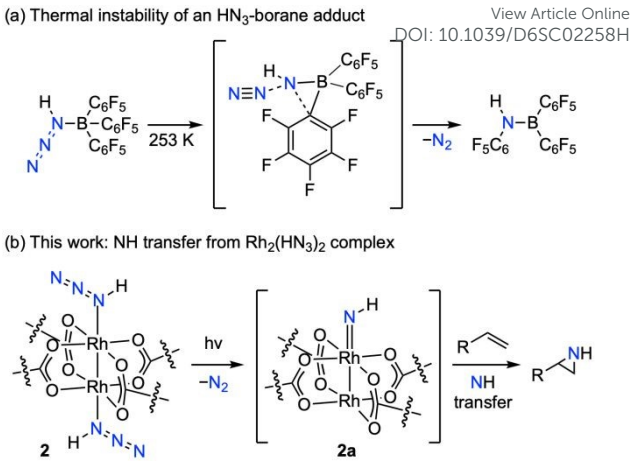

Figure 2. (a) $HN_3{\cdot}B(C_6F_5)_3$, the only previously reported crystalline HN_3 adduct, rearranges above 253 K. (b) Here, we report the synthesis, characterization, and imidogen-transfer photochemistry of $Rh_2(esp)_2(HN_3)_2$ (**2**), the first crystalline transition metal complex of HN_3.

Results and Discussion

Synthesis and Characterization. *$Rh_2(esp)_2(HN_3)_2$ (**2**).* HN_3 was prepared by the addition of stearic acid to solid NaN_3 (**SAFETY**: HN_3 is an explosive, toxic, and volatile substance; see Figures S1 and S2 for detailed synthetic protocol).[24, 25] Vacuum transfer of HN_3 to a CH_2Cl_2 solution of **1** resulted in a color change from light green to dark green. Diffraction-quality crystals of **2** were obtained by cooling this reaction solution to –20 °C. Refinement of the resulting SCXRD data revealed an N_α-coordination of HN_3 to both apical sites of $Rh_2(esp)_2$ (Figure 3a). The Rh(1)–Rh(2) bond distance for **2** is 2.382(1) Å (*c.f.*, for **1**, Rh–Rh is 2.3817(9)[40]) and the Rh(1)–N(1) distance is 2.317(2) Å, which is similar to previously reported aryl and alkyl azide complexes of Rh_2.[41, 42] The N–N–N bond angle (172.2(3)°) and the N(1)–N(2) and N(2)–N(3) bond lengths (1.246(3) and 1.122(3) Å, respectively) of **2** are similar to those of $(HN_3)_4$.[33]

The solid-state IR spectrum of **2** (ATR) features a broad N–H peak at 3212 cm^{-1} and two peaks at 2143 cm^{-1} and 1176 cm^{-1} corresponding to the asymmetric and symmetric azide stretches, respectively (Figure 3b). For comparison, we also prepared ^{2}H- and ^{15}N-labeled **2** (*i.e.*, [^{2}H]-**2** and [^{15}N]-**2**) by vacuum transfer of DN_3 and $H^{15}NN_2$, respectively. [^{15}N]-**2** displays solid-state IR features that are slightly red-shifted compared to **2** at 3196 cm^{-1}, 2119 cm^{-1}, and 1166 cm^{-1} (Figure 3b). [^{2}H]-**2** displays an N–D stretch at 2388 cm^{-1} (compared with an N–H stretch at 3112 cm^{-1} for **2**) and no significant perturbation of the azide stretching modes.

The ^{1}H NMR spectrum of **2** displays diamagnetically shifted peaks that integrate as expected for 2:1 coordination of HN_3 to **1**. The N–H chemical shift of **2** is temperature and concentration dependent (*vide infra*), but in general is sharper and shifted downfield compared to HN_3 (Figure 3c). For example, the N–H resonance of **2** is at 4.95 ppm (FWHM = 23.9 Hz) in CD_2Cl_2 at 298 K; the N–H resonance of HN_3 is at 4.52 ppm (FWHM = 61.1 Hz). The N–H resonance is also solvent dependent: The N–H chemical shift of **2** is at 4.95 ppm in CD_2Cl_2, 3.6 ppm in toluene-d_8 (Figure S3), and 3.2 ppm in the solid state (measured via magic angle spinning (MAS) solid-state (SS) [^{2}H]-NMR of [^{2}H]-**2** (Figure S4)). Finally, the ^{1}H spectrum of [^{15}N]-**2** displays a doublet for the N–H peak ($J_{N–H}$ = 69.0 Hz) (Figure 3c). The ^{1}H-coupled ^{15}N NMR spectrum of [^{15}N]-**2** displays two peaks: A singlet at –171.2 ppm and a doublet at –325.2 ppm ($J_{H–N}$ = 69.7 Hz), which we assign as γ-N and α-N, respectively (Figures 3d). The MAS-SS [^{15}N]-NMR of [^{15}N]-**2** displays analogous features at –159.1 and –336.7 ppm (Figure S5).

*$Rh_2(esp)_2(ArN_3)_2$ (**3**).* Treatment of complex **1** with PhN_3, 4-Me-C_6H_4–N_3, and 4-CF_3-C_6H_4–N_3 afforded aryl azide complexes **3a**-**c**. Dark green diffraction-quality crystals of **3a**-**c** were obtained by layering CH_2Cl_2 or $CHCl_3$ solutions of with pentane at –20 °C. Complexes **3** are structurally analogous to **2**: SCXRD analysis for all three compounds shows N_α-coordination of ArN_3 to the axial sites of $Rh_2(esp)_2$ (**1**) (Figure 4). The Rh(1)–N(1) bond distances of **3a**-**c** are 2.261(2) Å, 2.300(2) Å, and 2.271(3) Å (avg.) (there are two molecules of **3c** in the asymmetric unit), respectively, and ~0.1 Å shorter than the Rh(1)–N(1) bond of **2**. ^{1}H NMR data of **3a**-**c** confirms 2:1 coordination of the aryl azide ligands to **1**; during solvent removal from **3c**, partial loss of the apical azides was evident by integration of the ^{1}H NMR spectrum. The solid-state IR spectra display features azide stretches at ~2100 and ~2130 cm^{-1} for **3a**-**3c** (Figure S6).[43]

Ligand Binding Thermodynamics. The HN_3 ligands of **2** are labile in solution. The N–H chemical shift in the ^{1}H NMR of **2** is temperature (and concentration) dependent and shifts downfield upon cooling from 298 K to 203 K (Figure 5a). Similar

View Article Online
DOI: 10.1039/D6SC02258H

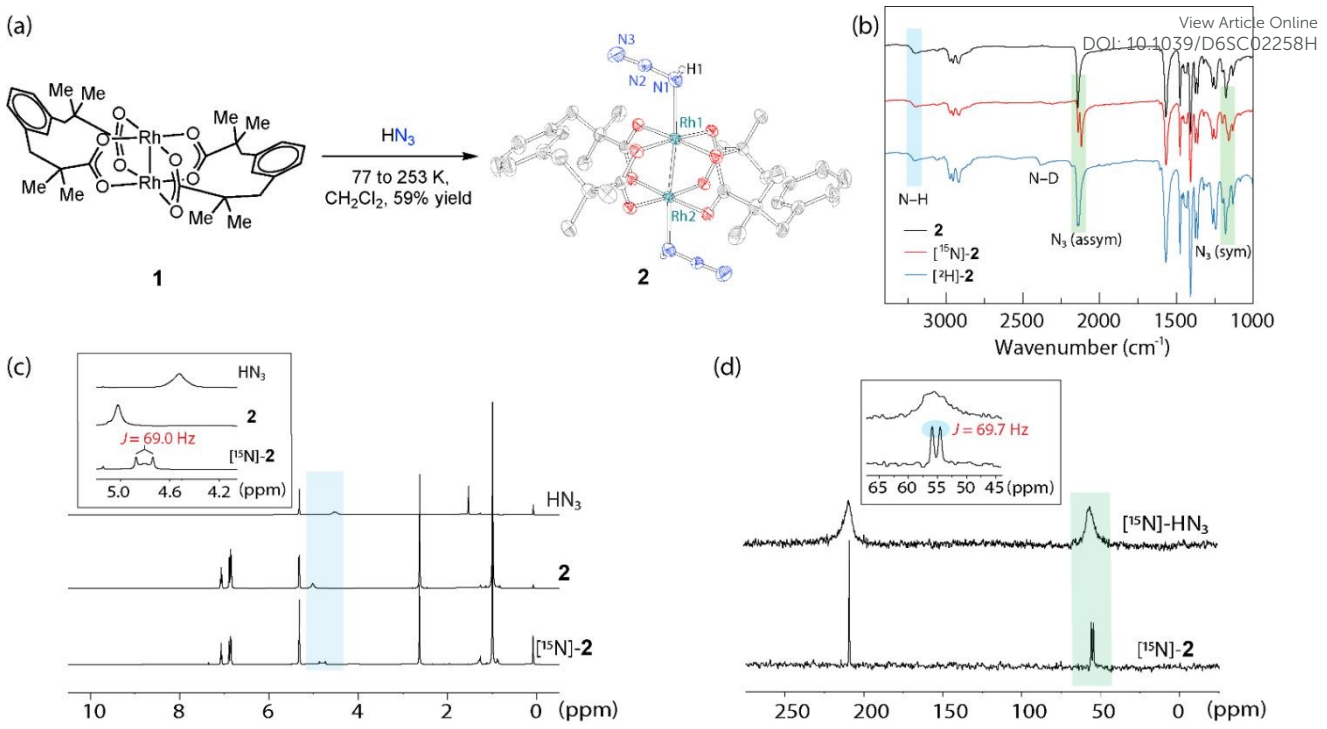

Figure 3. (a) Treatment of $Rh_2(esp)_2$ (**1**) with HN_3 affords $Rh_2(esp)_2(HN_3)_2$ (**2**). Displacement ellipsoid plot of **2** plotted at 50% probability; data were collected at 100 K. H-atoms, except H1, and CH_2Cl_2 are removed for clarity. Selected metrics: Rh(1)–Rh(2): 2.382(1) Å, Rh(1)–N(1): 2.317(2) Å, N(1)–N(2): 1.246(3) Å, N(2)–N(3):1.122(3) Å, N(1)–N(2)–N(3): 172.2(3)°. (b) Solid-state IR spectra of **2** (black trace), [^{15}N]-**2** (red trace), and [^{2}H]-**2** (blue trace) plotted from 3500 cm^{-1} to 1000 cm^{-1}. The blue shaded area highlights peak shift of the N–H stretch, and the green shaded area compares azide stretches for compounds **2**, [^{15}N]-**2**, and [^{2}H]-**2**. (c) ^{1}H NMR spectra of HN_3, **2**, and [^{15}N]-**2**; the concentration-dependent N–H resonances are highlighted in blue. Inset: Expansion highlighting the N–H resonances. (d) Proton-coupled ^{15}N NMR spectra of [^{15}N]-HN_3 and [^{15}N]-**2**; the ^{15}N resonances attributable to the N–H are highlighted in green. Inset: Peak splitting for [^{15}N]-**2** due to the ^{15}N-^{1}H coupling (J = 69.7 Hz).

temperature dependence is reflected in VT-^{15}N NMR experiments (Figure S7)**.** VT-IR spectroscopy similarly indicates facile equilibration of **2** and **1** + HN_3 (Figure 5b): A CH_2Cl_2 solution of **2** displays two azide stretching frequencies at 273 K — at 2138 and 2151 cm^{-1} — which we assign to HN_3 and **2**, respectively (in the solid-state the azide stretches for **2** appears at 2143 cm^{-1}).[44,45] Upon cooling, the relative intensity of these spectral features changes, with the free HN_3 stretch decreasing in intensity while the coordinated HN_3 stretch increases in intensity. Similar temperature dependence is noted in analysis of the symmetric vibrational mode and in VT-UV-vis measurements (Figure S8 and S9).

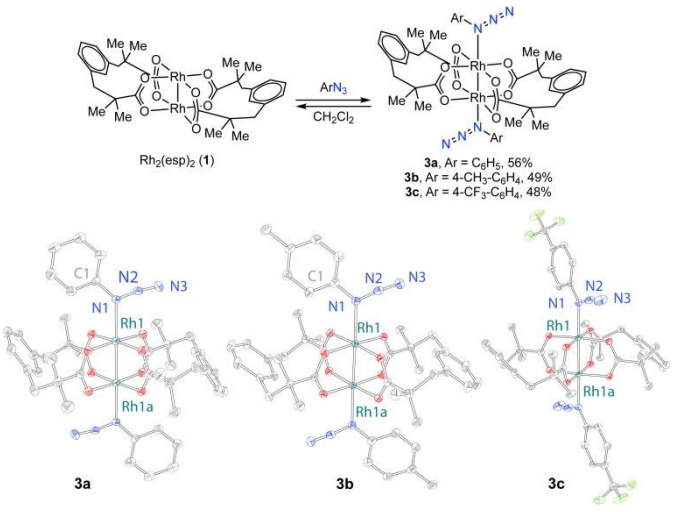

Figure 4. Synthesis and characterization of dirhodium aryl azide compounds **3.** Solid-state structure of compounds **3a**-**c**. Displacement ellipsoid plots of **3a**-**c** plotted at 50% probability; data were collected at 100 K. H-atoms and solvents of crystallization are removed for clarity. Selected metrics: Rh(1)–N(1): 2.261(2) Å for **3a**, 2.301(2) Å for **3b**, and 2.271(3) Å (avg.) for **3c**.

To evaluate the thermodynamics of HN_3 binding, we carried out an NMR titration of HN_3 with **1** at 243 K (–30 °C). The N–H resonance of HN_3 is systematically shifted downfield with increasing [**1**] (Figure S10). Using equations derived analogously to those of Drago,[46] these data enabled determination of temperature-dependent equilibrium constants (K_{eq}): K_{eq} = 1100 ± 100 M^{-2} at 243 K; K_{eq} = 120 M^{-2} at 298 K. Van't Hoff analysis (Figure S11), based on the obtained temperature-dependent equilibrium constants, provided ΔH^0 = –5.5 ± 0.1 kcal/mol and ΔS^0 = –9.0 ± 0.6 cal/K·mol. The K_{eq} for HN_3 binding is similar to that determined by Albrecht for the coordination of AdN_3 to $Fe(HMDS)_2$ (62 M^{-1} at 298 K) (Ad = adamantyl).[44]

We similarly carried out an NMR titration of PhN_3 with **1** (Figure S12) to evaluate the thermodynamics of aryl azide binding. The obtained data provided K_{eq} = 11000 ± 3000 M^{-2} at 243 K (K_{eq} = 2700 M^{-2} at 298 K), which is slightly larger than that measured for HN_3 (for VT-NMR of compound **3a**, see Figure S13). The relative binding affinities are consistent with enhanced Lewis basicity of Ph–*N*–N_2 as compared with H–*N*–N_2.[47] Van't Hoff analysis, based on K_{eq} measurements from 298

View Article Online
DOI: 10.1039/D6SC02258H

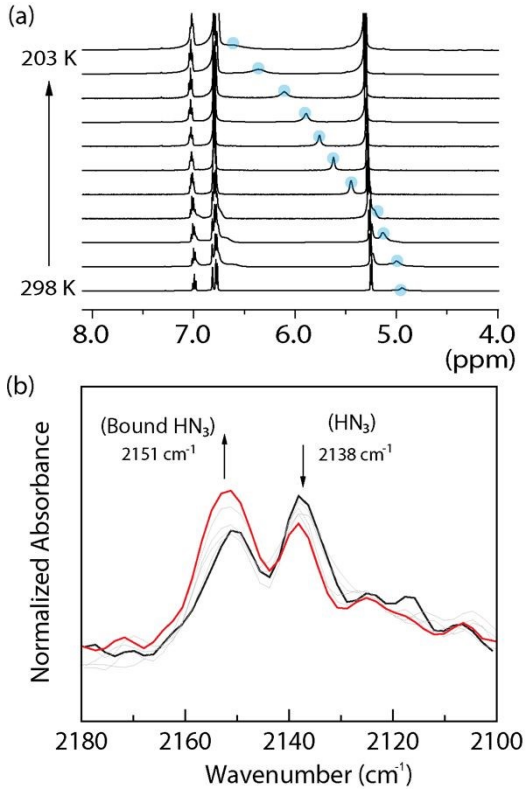

Figure 5. (a) VT-^{1}H NMR spectra of **2** collected in CD_2Cl_2 from 298 K to 203 K. The N–H resonance is highlighted in blue. (b) Solution-phase VT-IR spectra of **2** collected in CD_2Cl_2 from 273 K (black) to 233 K (red).

K to 203 K provided $\Delta H^0 = -4.23 \pm 0.06$ kcal/mol and $\Delta S^0 = 1.5 \pm 0.2$ cal/K·mol (Figure S14). Temperature-dependent UV-vis spectroscopic data of **3a**-**c** are collected in Figure S15. In comparison to common nitrogen donors, such as pyridine and acetonitrile ($K_{eq} > 10^3$ for binding to Rh_2), HN_3 and aryl azides are weakly binding ligands.[48-51]

NH-Transfer Photochemistry. To chemically evaluate the competence of photochemically generated intermediates to engage is N–H transfer, we pursued study of the NH-transfer photochemistry of **2** with olefinic substrates. Photolysis (λ = 300 nm, 243 K, quartz reaction vessel) of a CD_2Cl_2 solution of **2** in the presence of 1-octene resulted in NH transfer to afford the corresponding N–H aziridine (**4**) in 39% yield (Figure 6); compound **1** is observed as the Rh-containing byproduct by ^{1}H NMR (for ^{1}H and ESI-MS analysis see Figures S16 and S17). Similarly, photolysis of [^{15}N]-**2** in the presence of 1-octene affords a 1:1 mixture of **4**:[^{15}N]-**4**, which is expected from a mono-labeled [^{15}N]-HN_3 precursor (Figures S18 and S19). In this experiment, [^{15}N]-N_2 was also observed by ^{15}N-NMR (–70.3 ppm),[52] which demonstrates the facility of N_2 photoelimination under these reaction conditions (Figure S20). NH transfer to 1-octene was also observed for photolysis of a toluene solution, albeit in lower yield (12%), which we attribute to limited solubility of **2** at low temperature in this solvent (Figure S21). For comparison, photolysis of a CD_2Cl_2 solution of HN_3 and 1-octene in the absence of **1** did not give rise to any observable NH-transfer products (Figure S22).

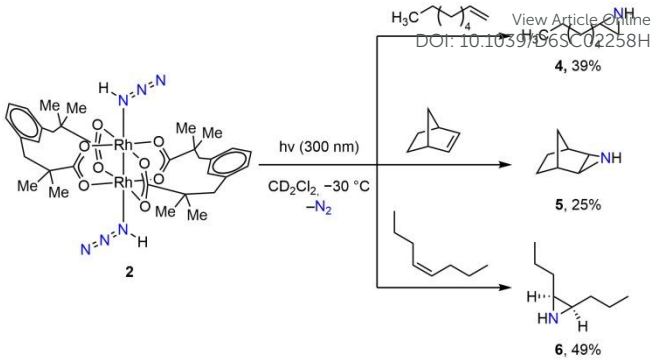

Figure 6. N–H transfer photochemistry of **2** with olefins. Photochemical olefin aziridination by **2** is stereospecific. Yields obtained by ^{1}H NMR spectroscopy.

Photolysis of **2** in the presence of norbornene affords the corresponding N–H aziridine **5** in 25% yield (for ^{1}H and ESI-MS analysis see Figures S23 and S24).[53] Photochemically promoted N–H transfer is stereospecific: Photolysis of **2** in the presence of *cis*-4-octene afforded *cis*-**6** exclusively (49% yield) (for ^{1}H and ESI-MS analysis see Figures S25 and S26). This observation is consistent with the stereospecific NH transfer that has been noted in Rh_2-catalyzed imidogen-transfer reactions.[14, 15] The modest yields of aziridines in these reactions are likely due to competing reaction of free NH with olefins: *N*-chloromethylamine was also observed as reaction byproducts (Figures S27-S29).[13, 54,55]

In contrast to the observed NH-transfer photochemistry from **2**, photolysis of **3a**-**3c** in the presence of 1-octene did not result in nitrene transfer products (*i.e.*, *N*-aryl aziridines or allylic amination products). This observation is consistent with facile intramolecular rearrangement of aryl nitrenes.[56]

Together, the results of these NH-transfer experiments indicate that the photogenerated intermediate from **2** is chemically and kinetically competent as an intermediate in the Rh_2-catalyzed NH-transfer.

Observation of Reactive Nitrenes. *Cryogenic photolysis of **2**.* Given the observation of imidogen transfer photochemistry from **2**, we sought to observe the putative Rh_2–NH intermediate (*i.e.*, **7**, Figure 7a). To this end, we carried out photolysis of a 2,2-dimethylbutane (DMB): *tert*-butylbenzene (TBB) (3:1) glass of **2** at 77 K in a quartz J-Young EPR tube. This solvent system was chosen to provide an optical glass while avoiding ligand exchange with more common glassy solvents such as 2-methyltetrahydrofuran.[57] Photolysis of **2** at 77 K results in a small but reproducible blue shift of the absorbance centered at 570 nm to 560 nm and the concurrent growth of significant spectral intensity ~500 nm (Figure 7b). These spectral features arise from a non-steady state intermediate: Thermal annealing of the sample to 298 K followed by re-freezing at 77 K results in the disappearance of the spectral intensity at 500 nm and the growth of a new absorbance centered at 543 nm, which overlays the spectrum of $Rh_2(esp)_2$ (**1**) in this solvent mixture (Figures S30 and S31). We carried out analogous cryogenic photolysis of [^{15}N]-**2** in a 3:1 DMB:TBB glass with the addition of 1-octene. Spectra obtained during this photolysis indicated the formation of the same non-steady state intermediate observed

View Article Online
DOI: 10.1039/D6SC02258H

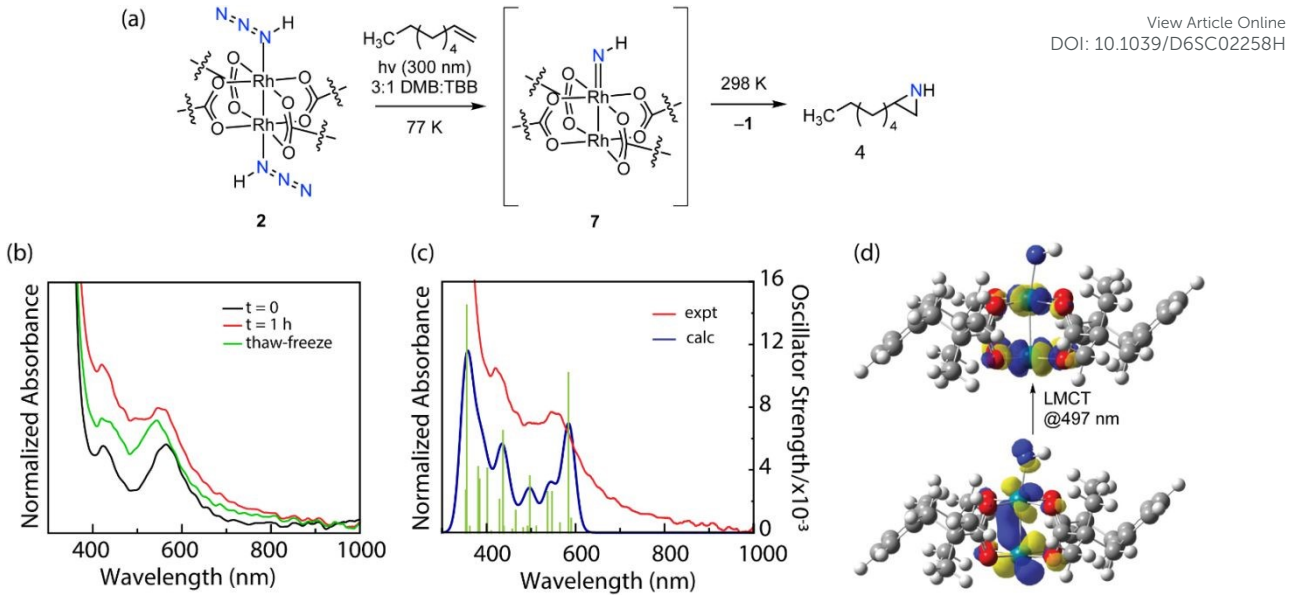

Figure 7. (a) Cryogenic photolysis (λ = 300 nm) of complex **2**. (b) UV-vis spectra of **2** (black), **7** (*i.e.*, after 1 h photolysis, red), and after thermal annealing (green) collected at 77 K. (c) UV-vis spectrum of **7** at 77 K (red) overlaid with the simulated spectrum of compound **7** (blue) based on the ^{3}TD-^{3}DFT calculation by PBE0-D3-BS1 method. Vertical transition pictured in green. (d) Principal NTOs for the transition at 497 nm.

in the absence of 1-octene (Figure S32). Thermal annealing of this sample led to disappearance of the non-steady state intermediate and the evolution of a 1:1 mixture of **4** and [^{15}N]-**4**, which demonstrates NH-transfer reactivity from the observed non-steady state intermediate (Figure S33).

We assign the non-steady state intermediate observed during 77 K photolysis to Rh_2–NH complex ^{3}[**7**]. The spectral features observed after cryogenic photolysis of **2** are consistent with TD-DFT calculations of ^{3}[**7**] (Figure 7c).[58] DFT single points of the singlet and triplet imidogen complexes (*i.e.* ^{1}[**7**] and ^{3}[**7**] at the SMD-PBE0-D3/Def2-TZVP level of theory) were used to calculate the ΔE_{ST} ($\Delta E_{ST} = E_{Singlet} - E_{Triplet}$) to be 11.9 kcal mol^{-1}. To further confirm this, single points at the DLPNO-CCSD(T)/Def2-TZVP level of theory were run and provided a ΔE_{ST} of 15.2 kcal mol^{-1}. The TD-DFT calculations of **2** and ^{3}[**7**], using *tert*-butylbenzene as an implicit solvent model, suggest that conversion of **2** to ^{3}[**7**] should be accompanied by minor changes in the absorbances at ~570 and ~425 nm but also the emergence of a new LMCT transition at 497 nm (Figure 7d).[59] This computed transition is well-matched to the growth of intensity observed experimentally at 500 nm (Figure S34). In contrast, the observed spectral features are not well-matched to the computed spectrum of ^{1}[**7**] (Figure S35). Further, the observed spectral features are inconsistent with the formation of Rh_2(II,III), which typically display low energy UV-vis transitions.[35,36]

Formulation as ^{3}[**7**] is consistent with the metrical parameters that we previously reported for triplet adamantyl and biaryl nitrenes of Rh_2 obtained by *in crystallo* photochemistry.[40,60-62] Attempts to accomplish *in crystallo* synthesis of **7** were not productive due to loss of crystallinity during sample photolysis.

*Cryogenic photolysis of **3a-3c**.* Guided by the hypothesis that *N*-arylation would provide a handle to modulate the electronic

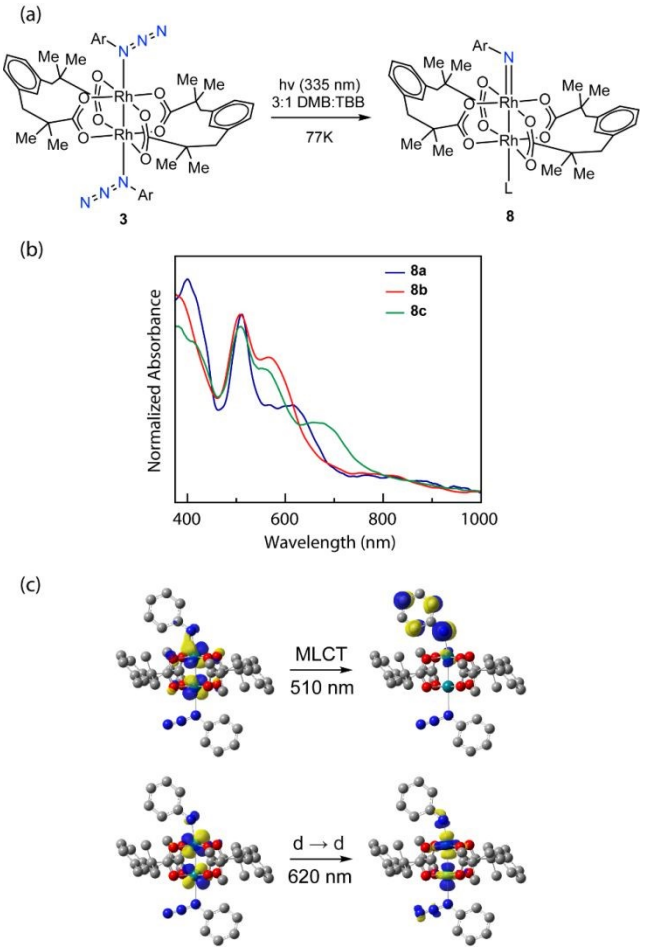

Figure 8. (a) Photolysis (λ = 335 nm) of complexes **3** at 77 K generates *N*-aryl nitrenes **8**. (b) UV-vis spectra of **8a** (red), **8b** (blue), and **8c** (green) collected at 77 K. (c) Principal NTOs for the transitions at 510 nm and 620 nm of ^{3}[**8a**].

absorption spectra of the resulting nitrene, we carried out the cryogenic photolysis of aryl azide complexes **3a**-**3c** (Figure 8a and 8b). Photolysis of **3a** in a 3:1 DMB:TBB glass at 77 K gave rise to a new absorption features centered at 510 nm and 620 nm. Thermal annealing led to the disappearance of these spectroscopic features. Similar to **7**, the experimental UV-vis spectra of **8a** was qualitatively similar to the TD-DFT simulated spectrum computed for a triplet nitrene although the simulated spectrum is blue-shifted as compared to experiment (for full spectral evolution see Figure S36). TD-DFT calculations of ^{3}[**8a**] show transitions with moderate oscillator strength (>0.01) at 469 nm and 516 nm (Figure S37a). Comparison of the simulated spectral shape and relative oscillator strengths suggests the transition at 469 nm corresponds to the sharper experimental feature at 510 nm whereas the transition at 516 nm corresponds to the feature at 620 nm. Natural Transition Orbital (NTO) analysis shows that the higher energy transition is MLCT from a Rh β d orbital into the SUMO that is delocalized between the nitrene N p orbital and the aryl group and the lower energy transition at 516 nm is mostly comprised of a Rh α d-to-d transition (Figure 8c, for all the NTOs of ^{3}[**8a**], see Figure S37b).

Cryogenic photolysis of **3b** also resulted in the evolution of a non-steady state intermediate (for full spectral evolution see Figure S38). The spectral features of ^{3}[**8b**] were observed at 507 nm and 571 nm and TD-DFT calculations result in a simulated spectrum (Figure S39a) that qualitatively aligns with experiment much like in the case of ^{3}[**8a**] and shows a blue shift for the higher energy peak relative to ^{3}[**8a**] (463 nm for ^{3}[**8b**] and 469 nm for ^{3}[**8a**]). NTO analysis indicates the parentage of these transitions is similar to those of the features observed for ^{3}[**8a**] (Figure S39b). The observed blue-shift of the peaks is consistent with methylation raising the energy of the acceptor orbital for the observed transitions. Superficially, the results obtained from cryogenic photolysis of **3c** also indicate the formation of a non-steady state intermediate (for full spectral evolution, see Figure S40). In this case however, evacuation of the solvent during the preparation of the glassy solvent matrix resulted in partial loss of the azide ligand (*vide supra*) and thus quantitative comparisons of the resulting optical spectrum are not possible (for TD-DFT and NTO analysis of ^{3}[**8c**], see Figure S41).

In crystallo photolysis of **3** provided experimental metrical parameters for the corresponding Rh_2 nitrenes (*i.e.*, ^{3}[**8a**], ^{3}[**8b**], and ^{3}[**8c**]) and confirmed the nitrene chemistry implied by the aforementioned spectroscopic and computational studies (Figure 9, for ^{3}[**8a**], and ^{3}[**8c**], see Figures S42 and S43). Photolysis of single crystals of **3** resulted in 30-50% photoconversion to the corresponding nitrenes before loss of crystallinity. In all cases, N_2 loss was associated with shortening of both the Rh(1)–N(1) bonds (*i.e.*, ~0.3 Å for Rh(1)–N(1)). Though we cannot locate the N_2 molecule *in crystallo* for **8a** and **8c** due to disorder, for **8b**, *in crystallo* photoextrusion of N_2 from **3b** was observed. The metrical parameters of **8a**, **8b**, and **8c** are consistent with formulation as triplet complexes. DFT single points at the SMD-PBE0-D3/Def2-TZVP level of theory were used to calculate the ΔE_{ST} to be 11.4 kcal mol^{-1}, 9.1 kcal mol^{-1}, and 12.4 kcal mol^{-1} for ^{3}[**8a**], ^{3}[**8b**], and ^{3}[**8c**], respectively.

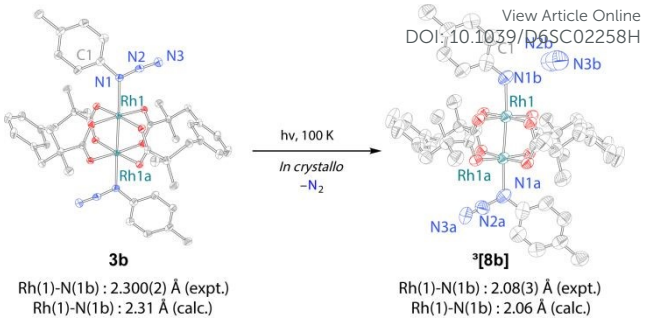

Figure 9. *In crystallo* characterization of ^{3}[**8b**], upon photo-extrusion of N_2 molecule from **3b** with 35% photoconversion. The obtained metrical parameters are well-matched to the optimized geometry for triplet *N*-aryl nitrene (*i.e.*, ^{3}[**8b**]).

Conclusions

Here, we describe the first structurally characterized transition metal complex of hydrazoic acid, $Rh_2(esp)_2(HN_3)_2$ (**2**), by addition of gaseous HN_3 to $Rh_2(esp)_2$ (**1**). Temperature-dependent NMR, UV-vis, and IR measurements indicate that the HN_3 ligands are labile in solution; $K_{eq} = 1100 \pm 100$ M^{-2} at 243 K. Complex **2** engages in stereospecific NH-transfer photochemistry with olefins, which suggests that the same intermediate is accessed during photolysis of **2** as is generated during Rh_2-catalyzed NH-transfer reactions.[9] Cryogenic photolysis of **2** in a frozen solvent glass enabled observation of the transient Rh_2–NH intermediate. Comparison of the spectroscopic data with results of DFT and TD-DFT calculations suggest this intermediate displays a triplet ground state (*i.e.*, ^{3}[**7**]).

Analogous aryl azide complexes provided further support for the structural and spectroscopic assignments in the hydrazoic acid photochemistry. Cryogenic UV-vis spectroscopy provided evidence for the intermediacy of ^{3}[Rh_2–NAr] complexes and bolstered the computationally supported spectroscopic assignments for ^{3}[Rh_2–NH]. In addition, *in crystallo* synthesis provided experimental definition of the metrical parameters of the aryl nitrene adducts, which both confirms the nitrene photochemistry of this family of azide complexes as well as further supports the formulation as triplet adducts. Together, these results introduce HN_3 as a ligand in transition metal coordination chemistry, enable photochemical generation of M–NH species, and provide new tools to study metal-catalyzed amination chemistry.

Author contributions

A.P., G.P.V.T., and D.C.P conceptualized the project. A.P, P.T., M.T.F., B.M., M.J.L., J.H.R., and G.P.V.T. carried out experimental work. The manuscript was written with contributions from all authors.

Conflicts of interest

There are no conflicts to declare.

Data availability

Experimental details and spectral data are available in the Supplementary Information. X-ray diffraction data has been deposited in the Cambridge Crystallographic Data Centre (CCDC).

Acknowledgements

The U.S. Department of Energy (DOE), Office of Science, Office of Basic Energy Sciences, Catalysis Program (DE-SC0024121) and the Welch Foundation (A-1907) are acknowledged for funding. Texas A&M University HPRC provided computational resources (https://hprc.tamu.edu).

References

1. Klima, R. F.; Gudmundsdóttir, A. D. *J. Photochem. Photobiol. A*, 2004, **162**, 239–247.
2. Gritsan, N. P.; Platz, M. S. *Chem. Rev.*, 2006, **106**, 3844–3867.
3. Wang, D.; Chen, W.; Chen, H.; Chen, Y.; Ye, S.; Tan, G. *Nat. Chem.*, 2024, **17**, 38–43.
4. Janssen, M.; Frederichs, T.; Olaru, M.; Lork, E.; Hupf, E.; Beckmann, J. *Science*, 2024, **385**, 318–321.
5. Jia, Z.-J.; Gao, S.; Arnold, F. H. *J. Am. Chem. Soc.*, 2020, **142**, 10279–10283.
6. Anugu, R. R.; Munnuri, S.; Falck, J. R. *J. Am. Chem. Soc.*, 2020, **142**, 5266–5271.
7. Boullé, A.; Doumbia, A.; Mahy, J.-P.; Avenier, F. *Chem. Commun.*, 2023, **59**, 79–81.
8. Jat, J. L.; Chandra, D.; Kumar, P.; Singh, V.; Tiwari, B. *Synthesis*, 2022, **54**, 4513–4520.
9. Y. Gelato, L. Marraffa, F. Pasca, P. Natho, G. Romanazzi, A. Tota, M. Colella and R. Luisi, *J. Am. Chem. Soc.*, **2025**, *147*, 35567–35575.
10. Amble, E.; Dailey, B. P. *J. Chem. Phys.*, 1950, **18**, 1422.
11. Dimerization of ^{3}[NH] to generate ^{1}[HN–NH] is a spin-allowed reaction according to the Carter-Goddard-Malrieu-Trinquier (CCMT) rules; see, Driess, M.; Grützmacher, H. *Angew. Chem. Int. Ed.*, 1996, **35**, 828–856 and Power, P. *Chem. Rev.*, 1999, **99**, 3463–3504.
12. Jacox, E.; Milligan, D. E. *J. Am. Chem. Soc.*, 1963, **85**, 278–282.
13. Cornell, D. W.; Berry, R. S.; Lwowski, W. *J. Am. Chem. Soc.*, 1966, **88**, 544–550.
14. Ma, Z.; Zhou, Z.; Kürti, L. *Angew. Chem. Int. Ed.*, 2017, **56**, 9886–9890.
15. Jat, J. L.; Paudyal, M. P.; Gao, H.; Xu, Q.-L.; Yousufuddin, M.; Devarajan, D.; Ess, D. H.; Kürti, L.; Falck, J. R. *Science*, 2014, **343**, 61–65.
16. Xue, W.; Zhu, Z.; Chen, S.; You, B.; Tang, C. *J. Am. Chem. Soc.*, 2023, **145**, 4142–4149.
17. Mao, R.; Gao, S.; Qin, Z.-Y.; Rogge, T.; Wu, S. J.; Li, Z.-Q.; Das, A.; Houk, K. N.; Arnold, F. H. *Nat. Catal.*, 2024, **7**, 585–592.
18. Fan, F.-X.; Xu, H.; Tang, S.-X.; Dang, Y.; Wang, F. *Nat. Commun.*, 2025, **16**, 1471.
19. Curtius, T. *Ber. Dtsch. Chem. Ges.*, 1890, **23**, 3023–3033.
20. Eyster, E. H. *J. Chem. Phys.*, 1940, **8**, 135–142.
21. Schomaker, V.; Spurr, R. *J. Am. Chem. Soc.*, 1942, **64**, 1184–1187.
22. Kajimoto, O.; Yamamoto, T.; Fueno, T. *J. Phys. Chem.*, 1979, **83**, 429–435.
23. Lievin, J.; Breulet, J.; Verhaegen, G. *Theor. Chim. Acta*, 1979, **52**, 75–88.
24. Evers, J.; Oehlinger, G.; Steemann, F. X.; Klapötke, T. M. *Inorg. Chem.*, 2020, **59**, 17671–17677.
25. Evers, J.; Göbel, M.; Krumm, B.; Martin, F.; Medvedyev, S.; Oehlinger, G.; Steemann, F. X.; Troyan, I.; Klapötke, T. M.; Eremets, M. I. *J. Am. Chem. Soc.*, 2011, **133**, 12100–12105.
26. Himmel, H.-J.; Junker, M.; Schnöckel, H. *J. Chem. Phys.*, 2002, **117**, 3321–3326.
27. Laursen, S. L.; Grace, J. E.; DeKock, R. L.; Spronk, S. A. *J. Am. Chem. Soc.*, 1998, **120**, 12583–12594.
28. Russell, J. N.; Bermudez, V. M.; Leming, A. *Langmuir*, 1996, **12**, 6492–6500.
29. Schmidt, A. *Z. Anorg. Allg. Chem.*, 1971, **381**, 31–39.
30. Morán, M.; Gayoso, M. *J. Organomet. Chem.*, 1983, **243**, 423–426.
31. Schäfer, H.; Saak, W.; Weidenbruch, M. *J. Organomet. Chem.*, 2000, **604**, 211–213.
32. Brown, Z. D.; Erickson, J. D.; Fettinger, J. C.; Power, P. P. *Organometallics*, 2013, **32**, 617–622.
33. Bläsing, K.; Bresien, J.; Labbow, R.; Michalik, D.; Schulz, A.; Thomas, M.; Villinger, A. *Angew. Chem. Int. Ed.*, 2019, **58**, 6540–6544.
34. Lorpitthaya, R.; Xie, Z.-Z.; Sophy, K. B.; Kuo, J.-L.; Liu, X.-W. *Chem. Eur. J.*, 2010, **16**, 588–594.
35. Lin, X.; Zhao, C.; Che, C.-M.; Ke, Z.; Phillips, D. L. *Chem. Asian J.*, 2007, **2**, 1101–1108.
36. Kornecki, K. P.; Berry, J. F. *Chem. Eur. J.*, 2011, **17**, 5827–5832.
37. Zalatan, D. N.; Du Bois, J. *J. Am. Chem. Soc.*, 2009, **131**, 7558–7559.
38. Perry, R. H.; Cahill, T. J.; Roizen, J. L.; Du Bois, J.; Zare, R. N. *Proc. Natl. Acad. Sci. U. S. A.*, 2012, **109**, 18295–18299.
39. Bishnoi, P.; Singh, A.; Maurya, Y.; Jhamb, V.; Sharma, A.; Sivapreetha, S. V.; Chatterjee, S. *ACS Org. Inorg. Au*, 2025, **5**, 385–399.
40. Espino, C. G.; Fiori, K. W.; Kim, M.; Du Bois, J. *J. Am. Chem. Soc.*, 2004, **126**, 15378–15379.
41. Das, A.; Chen, Y.-S.; Reibenspies, J. H.; Powers, D. C. *J. Am. Chem. Soc.*, 2019, **141**, 16232–16236.
42. Das, A.; Van Trieste, G. P.; Powers, D. C. *Comments Inorg. Chem.*, 2020, **40**, 116–158.
43. Das, A.; Wang, C.-H.; Van Trieste, G. P.; Sun, C.-J.; Chen, Y.-S.; Reibenspies, J. H.; Powers, D. C. *J. Am. Chem. Soc.*, 2020, **142**, 19862–19867.
44. Stroek, W.; Keilwerth, M.; Malaspina, L. A.; Grabowsky, S.; Meyer, K.; Albrecht, M. *Chem. Eur. J.*, 2024, **30**, e202303410.
45. Analogous VT-IR experiments were used to characterize the binding equilibrium of adamantyl azide (AdN_3) with $Fe(HMDS)_2$.
46. Drago, R. S. *Physical Methods for Chemists*; Saunders College Publishing, 1992.
47. Hunter, E. P. L.; Lias, S. G. *J. Phys. Chem. Ref. Data*, 1998, **27**, 413–656.
48. Drago, R. S.; Tanner, S. P.; Richman, R. M.; Long, J. R. *J. Am. Chem. Soc.*, 1979, **101**, 2897–2903.
49. Drago, R. S.; Long, J. R.; Cosmano, R. *Inorg. Chem.*, 1981, **20**, 2920–2927.
50. Drago, R. S.; Long, J. R.; Cosmano, R. *Inorg. Chem.*, 1982, **21**, 2196–2202.
51. Trindade, A. F.; Coelho, J. A. S.; Afonso, C. A. M.; Veiros, L. F.; Gois, P. M. P. *ACS Catal.*, 2012, **2**, 370–383.
52. Banert, K.; Singh, N.; Fiedler, B.; Friedrich, J.; Korb, M.; Lang, H. *Chem. Eur. J.*, 2015, **21**, 15092–15099.
53. Photopolymerization of styrenes upon UV irradiation prevented evaluation of potential N–H transfer to these substrates.

View Article Online
DOI: 10.1039/D6SC02258H

54. Kodama, S. *Bull. Chem. Soc. Jpn.*, 1983, **56**, 2363–2370.
55. Attempts to achieve photocatalysis by carrying out photolysis of solutions of **1** with excess HN_3 and olefinic substrates were unsuccessful, presumably due to preferential product binding to **1**.
56. Inui, H.; Sawada, K.; Oishi, S.; Ushida, K.; McMahon, R. J. *J. Am. Chem. Soc.*, 2013, **135**, 10246–10249.
57. Suslick, K. S.; Bautista, J. F.; Watson, R. A. *J. Am. Chem. Soc.*, 1991, **113**, 6111–6114.
58. ^{3}[**7**] is presumably generated from **2** by initial excitation to a singlet excited state that undergoes intersystem crossing to a triplet excited state from which N_2 dissociation proceeds.
59. The low energy feature at around 1100 nm was not observed as the spectrometer collection range was 100–1060 nm.
60. Paikar, A.; Van Trieste, G. P.; Das, A.; Wang, C.-W.; Sill, T. E.; Bhuvanesh, N.; Powers, D. C. *Inorg. Chem.*, 2023, **62**, 12557–12564.
61. Baek, Y.; Das, A.; Zheng, S.-L.; Reibenspies, J. H.; Powers, D. C.; Betley, T. A. *J. Am. Chem. Soc.*, 2020, **142**, 11232–11243.
62. Sur, A.; Powers, D. C. *ACS Cent. Sci.*, 2025, **11**, 8348–8352.

View Article Online
DOI: 10.1039/D6SC02258H

Experimental details and spectral data are available in the Supplementary Information. X-ray diffraction data has been deposited in the Cambridge Crystallographic Data Centre (CCDC).